

# Mechanisms of cooperativity underlying sequence-independent $\beta$ -sheet formation

Chinlin Guo, Margaret S. Cheung, Herbert Levine

*Department of Physics, University of California, San Diego*

*9500 Gilman Drive, La Jolla, CA 92093-0319*

David A. Kessler

*Department of Physics, Bar-Ilan University, Ramat-Gan, Israel*

(Dated: October 29, 2018)

## ABSTRACT

We investigate the formation of  $\beta$ -sheet structures in proteins without sequence-dependent side-chain interactions. To accomplish this, we introduce a model which explicitly incorporates both solvation effects and the angular dependence (on the protein backbone) of hydrogen bond formation. The thermodynamics of this model is studied by exploring the density of states for the entire system and the local couplings in a partially folded structure. Our results suggest that solvation dynamics together with the H-bond angular dependence gives rise to a generic cooperativity in this class of systems; this result explains why pathological aggregates involving  $\beta$ -sheet cores can form from many different proteins. Our work provides the foundation for the construction of phenomenological models to investigate topology effects in  $\beta$ -sheet folding and the competition between native folding and non-specific aggregation.

## I. INTRODUCTION

$\beta$ -sheets are an important element of protein structure, occurring often both in functional units and in pathological aggregates. For example, signaling proteins such as SH3 contain a  $\beta$  core. On the other hand, the precursors of amyloidogenesis are commonly found to have a  $\beta$ -sheet organization<sup>1</sup>; moreover, a conformational rearrangement can switch a functional  $\beta$ -sheet into an aggregation unit<sup>2,3</sup>. As they play the role of stabilizing highly organized

architectures (either pathological or functional),  $\beta$ -sheets must be strongly cooperative units, responsible for lowering the free energy of these folded structures as compared to entropy-dominated more irregular patterns.

It is often assumed that hydrophobic interactions are the major forces contributing to  $\beta$ -sheet cooperativity and their interacting pattern (i.e., the sequence design) can define a unique fold<sup>4</sup>. But, one cannot ignore the fact that many neurodegenerative diseases are caused by the aggregation of mutant proteins with long *hydrophilic* sequences (e.g., polyglutamine in Huntington disease<sup>5</sup>); the  $\beta$ -sheet at the core of these aggregates are certainly not being stabilized by hydrophobic forces. Indeed, recent experiments have shown that peptides with purely hydrophilic sequences can fold  $\beta$ -sheets cooperatively<sup>6</sup>. Also, growing evidence suggests that proteins are capable of forming  $\beta$ -sheet aggregates, regardless of their native folds<sup>7</sup>. Together with the fact that most amyloidogenic precursors do not share any homologous sequence<sup>1</sup>, it is therefore very likely that throughout the 2-dimensional  $\beta$ -sheet architecture, formation of an H-bond network can generate long-range ordering, hence compensating the mismatch of side-chain interactions and stabilizing the system.

What are the basic differences between backbone H-bond and side-chain hydrophobic interactions? Besides the difference in sequence specificity discussed above, they also differ in the maximal number of contacts for each interaction unit. Along the peptide chain, one amino acid can form at most two backbone H-bonds with adjacent  $\beta$ -strands in the 2-dimensional  $\beta$ -sheet structure. In contrast, for each hydrophobic residue in a compact protein, the number of favorable (sequence specific) contacts can be more than two; this leads to many-body effects that can define and stabilize a unique fold<sup>4,8,9</sup>. In most protein folding literature, the hydrophobic many-body effect is mimicked by the use of G $\ddot{o}$ -type interaction<sup>10</sup> and sequence-specific restrictions on the backbone energy<sup>11</sup> to favor the native state. This approach, however, is not generally applicable to the case of sequence-independent  $\beta$ -sheet formation.

Moreover, from a statistical mechanics prospective, it is well known that having cooperative behavior in a 2-dimensional, pairwise-interacting system requires more than two couplings (in average) for each interaction unit<sup>12</sup>. In protein folding, this corresponds to the case that folding of a specific part of the overall structure will aid its contiguous contact formation without redundant entropy loss, as briefly discussed by Berriz *et al*<sup>13</sup>. At the first glance, this principle does not apply to the case of H-bond network formation in an obvious

way. Thus, elucidating how the networking of individual H-bond can give rise to a stable folded structure is the major goal of present work.

For this purpose, we study a model system without specific side-chain interaction. It has already been shown that for  $\beta$ -structured proteins with randomly assigned sequences, a pure Lennard-Jones potential might not be sufficient to provide systemic cooperativity,<sup>14</sup> and angular dependence in contact formation must be taken into account<sup>13</sup>. Also, there is growing evidence that solvent effects play a significant role in protein folding and conformational changes<sup>15,16,17,18,19</sup>. Thus, we introduce a new approach to integrate these two effects in modeling H-bond formation. The ingredients of our approach are a “co-plane” parameterization of the backbone degrees of freedom with explicit couplings of solvation dynamics and the angular dependence of hydrogen-bond formation. The systemic cooperativity is investigated by exploring the density of states for  $\beta$ -sheets of different size and structure. To facilitate the sampling, we have used replica-exchange<sup>20</sup> and multi-canonical rescaling<sup>21</sup> techniques. The origin of this global cooperativity is further studied by comparing energetics and thermodynamic stability of local sub-structures of model systems with different types of interaction potentials.

Our results indicate that it is the de-solvation cavity formation (i.e., the granularity of the water molecule) and the hydrogen-bond angular dependence that provide  $\beta$ -sheets with a systemic cooperativity. Since this property is sequence-independent, our results suggest why  $\beta$ -sheets can generically serve as the building blocks for constructing functional macromolecules, and why most functional proteins have the tendency to form aggregates at sufficiently high concentration.

## II. METHOD

### A. The model system

The system proposed here is based on the “ball-and-stick” model introduced in Ref. 22. In this approach, all NH, C $_{\alpha}$ , CO (represented as C'), and C $_{\beta}$  side-chains are treated as lumped balls. The local backbone energy consists of a sum of terms:

1. bond bending:  $V_{\theta} = \frac{1}{2} \sum k_{\theta}(\theta_i - \theta_0)^2$

2. dihedral rotations:  $V_\omega = \frac{1}{2} \sum \epsilon_\omega (1 + \cos \omega_i)$ ,  $V_\phi = \frac{1}{2} \sum \epsilon_\phi (1 + \cos 3\phi_i)$ ,  $V_\psi = \frac{1}{2} \sum \epsilon_\psi (1 + \cos 3\psi_i)$ ,

3. side-chain chirality:  $V_{chiral} = \sum \epsilon_{chiral} \Theta \left( \{ [\hat{r}_{NC_\alpha} \times \hat{r}_{C_\beta C_\alpha}] \cdot \hat{r}_{C' C_\alpha} \}_i \right)$

with the sum taken over all components (labeled by  $i$ ), and  $\Theta(s) = (s + |s|)/2$ . Here, since we are interested in sequence-independent effects, all side-chains are treated as polar or weakly charged groups that favor  $\beta$ -sheet formation, with interaction strengths<sup>4,26</sup> that are far less than the magnitude of the H-bond energy and can be generally ignored. Also, we take the parameters  $k_\theta = 200 \text{kcal/mol} \cdot \text{rad}^2$ ,  $\epsilon_\omega = 40 \text{kcal/mol}$ ,  $\epsilon_\phi = \epsilon_\psi = 0.45 \text{kcal/mol}$ , and  $\epsilon_{chiral} = 10 \text{kcal/mol}$  from Ref. 22.

## B. The solvation force field

Next, we construct expressions for the non-local interactions. We incorporate the solvation effect into the force law by designing a double-well potential that can account for contact formation and single-H<sub>2</sub>O hydration (between the contact pair); the barrier between the wells corresponds to the free energy cost involved in the transfer of a water molecule out of the hydration shell<sup>15,23</sup>. Multiple shells could be accommodated via a multiple-well potential, but this is not attempted here. The approximation of using an effective free-energy is justified via the observation that transfer of water from within the vicinity of the contact pair is faster than the contact formation<sup>15,16,17,18</sup>.

There is no standard way to construct a continuous de/solvation potential<sup>24</sup> which can be used for Langevin simulations; we note that a previous curve fitting effort<sup>25</sup> and a recent Monte Carlo study<sup>23</sup> utilized a discrete version of such a potential. We therefore propose an empirical profile based on estimated experimental parameters. Specifically, we will take for H-bond formation

$$U_{\text{Hb}}(r) = \frac{A}{r^k} \left[ \frac{1}{4r^{3k}} - \left( \frac{1}{(r_{\text{Hb}}^c)^k} + \frac{1}{(r_{\text{Hb}}^*)^k} + \frac{1}{(r_{\text{Hb}}^{\text{sol}})^k} \right) \frac{1}{3r^{2k}} \right. \\ \left. + \left[ \left( \frac{1}{(r_{\text{Hb}}^c)^k} + \frac{1}{(r_{\text{Hb}}^*)^k} \right) \frac{1}{(r_{\text{Hb}}^{\text{sol}})^k} + \frac{1}{(r_{\text{Hb}}^c r_{\text{Hb}}^*)^k} \right] \frac{1}{2r^k} - \frac{1}{(r_{\text{Hb}}^c r_{\text{Hb}}^* r_{\text{Hb}}^{\text{sol}})^k} \right] \quad (1)$$

Here  $r$  is the distance between NH and CO, and the integer  $k \in N$  ( $k = 6$ , e.g.) is chosen to give specific long-range behavior. The values  $r = r_{\text{Hb}}^c$ ,  $r = r_{\text{Hb}}^*$ , and  $r = r_{\text{Hb}}^{\text{sol}}$  represent the

separation distance at the contact bond position, at the the peak of the desolvation barrier, and in the presence of a single intervening solvent molecule separation, respectively.  $r_{\text{Hb}}^{\text{sol}}$  is obtained by adding the known value of  $r_{\text{Hb}}^{\text{c}}$  to the size of a single  $\text{H}_2\text{O}$ .  $A$  and  $r_{\text{Hb}}^*$  can be determined by the strengths of the H-bond<sup>22</sup> and the desolvation barrier; the latter is approximated by the surface energy involved in forming a desolvation cavity, estimated to equal  $\approx 0.103\text{kcal}/(\text{mol } \overset{\circ}{\text{A}}^2)^{18}$ . Here we have  $r_{\text{Hb}}^{\text{c}} \approx 3.43 \overset{\circ}{\text{A}}$  and  $r_{\text{Hb}}^* \approx 3.92 \overset{\circ}{\text{A}}$ ; these yield a single  $\text{H}_2\text{O}$  hydration energy of  $\approx -0.5 \text{ kcal/mol}$ .

Clearly, the design principle behind this type of formula is to have three roots for  $dU_{\text{Hb}}(r)/dr = 0$  accounting for the desolvation barrier and for the two local minima; one can add more roots to address multiple solvation shell effects. Note that one might wish to fine-tune the potential profile more precisely (for instance, by being able to independently vary the width of the contact well). This can be accomplished by a more complicated expression (see appendix A). Also, the strength of de/solvation might depend on the hydrophobicity of local environment (i.e., de-wetting behavior) and one can certainly take this into account.

As discussed in<sup>22,26</sup>, hydrogen bond formation has a strong angular dependence on its surrounding backbone; thus, one can not fully describe the interaction using the radial distance alone. From Fig. 1(d), we note that such an angular dependence is merely the requirement that all atoms near to the interacting NH, CO (i.e. the shadowed area) are aligned “natively”. In Ref. 22, this “alignment” effect is accomplished by introducing artificial repulsive forces between H-bond neighbors. Here, we propose instead a “functional-block” (co-plane) scheme.

### C. The co-plane approach

From Fig. 1(a), we notice that the peptide backbone between two contiguous  $\text{C}_\alpha$  atoms has a co-planar structure because of the N-C-O bond resonance. This allows us to model the motion of a “co-plane” as a whole (i.e., with one dihedral angle  $\omega$  fixed to  $\approx 180^\circ$ ). Overall, each interacting unit in our system is just one block of  $\text{C}_\alpha$  co-plane. The  $i^{\text{th}}$  co-plane is defined by three points  $\{\text{X}_1^{(i)}, \text{X}_2^{(i)}, \text{X}_3^{(i)}\}$  where  $\text{X}_1^{(i)}, \text{X}_3^{(i)}$  are simply the two  $\text{C}_\alpha$  in the plane and  $\text{X}_2^{(i)}$  is a virtual point satisfying  $\overrightarrow{\text{X}_1^{(i)}\text{X}_2^{(i)}} \perp \overrightarrow{\text{X}_2^{(i)}\text{X}_3^{(i)}}$ , fig.1(b). Once the degree of freedom corresponding to this point is specified, all the atomic locations of the amide and carbonyl groups are fixed. Note that a convenient way to define the arbitrary point  $\text{X}_2$  is such that

the vector  $\overrightarrow{X_2^{(i)}X_3^{(i)}}$  points directly at the  $C_\alpha$  of the neighboring strand if the system is in the native  $\beta$ -sheet structure; see fig.1(c). Once  $X_2^{(i)}$  is chosen, this determines the in-plane angles  $\theta_1$  and  $\theta_2$  as well as the virtual plane projection angle  $\theta_3$ . We computed all these objects by using the native value of bond angles<sup>22</sup> and dihedral angles observed in regular  $\beta$ -sheets ( $\phi \sim -138 \pm 1^\circ$ ,  $\psi \sim 135 \pm 1^\circ$ )<sup>26</sup>. This leads to all geometrical properties of the virtual plane, including  $\theta_1 = 64.7^\circ$ ,  $\theta_2 = 62.2^\circ$ ,  $\theta_3 = 22.4^\circ$ ,  $\overline{X_1X_2} = 3.75 \text{ \AA}$ ,  $\overline{X_2X_3} = 0.57 \text{ \AA}$ .

Given the native plane, we define the range of possible non-native structures via allowing the orientation of the planes to vary. This yields three degrees of freedom per residue; two reflect the angles needed to define the direction of the fixed length vector going from one  $C_\alpha$  to the next while the third refers to a rolling of the plane around this vector. One can then work out the geometrical problem of expressing, in terms of these degrees of freedom, the residual terms in the backbone energy arising from the dihedral terms involving  $\phi$  and  $\psi$ , the bending of the bond angle  $\angle C'C_\alpha N$ , and the side-chain chiralities between consecutive blocks. Our approach fully maintains the overall translation and rotational degrees of freedom of the protein molecule. This co-plane parameterization greatly reduces our computation effort as compared to all atom backbones, yet maintains the roll degree of freedom not present in the simplified  $C_\alpha$  model. As will be shown later, this degree of freedom is important for the study of  $\beta$ -sheet cooperativity.

#### D. The structural factor

Now we use the co-plane approach to model the H-bond angular dependence. From fig.1(e), we note that having a H-bond between blocks  $i, j$  requires fixing two rotational and two translational degrees of freedom. More precisely, we need  $\overrightarrow{X_1^{(i)}X_2^{(i)}}$  antiparallel to  $\overrightarrow{X_1^{(j)}X_2^{(j)}}$ , and  $\overrightarrow{X_2^{(i)}X_3^{(i)}}$  parallel to  $\overrightarrow{X_2^{(j)}X_3^{(j)}}$ , whereas for translational alignment, the two sets of points  $\{X_1^{(i)}, X_2^{(j)}, X_3^{(j)}\}$  and  $\{X_1^{(j)}, X_3^{(i)}, X_2^{(i)}\}$  must be collinear. This leads us to define a structural factor that monitors the angular nativeness in the H-bond

$$x_{\text{Hb}}^{(i,j)} = \frac{1}{16} \left[ 1 - \widehat{X_{12}^{(i)}} \cdot \widehat{X_{12}^{(j)}} \right] \left[ 1 + \widehat{X_{23}^{(i)}} \cdot \widehat{X_{23}^{(j)}} \right] \times \left[ 1 + \cos \angle X_2^{(j)} X_1^{(i)} X_3^{(j)} \right] \left[ 1 + \cos \angle X_2^{(i)} X_1^{(j)} X_3^{(i)} \right] \quad (2)$$

where  $\widehat{X_{ab}^{(k)}}$  is the unit vector connecting  $X_a^{(k)}, X_b^{(k)}$ . Note that  $x_{\text{Hb}}^{(i,j)}$  has maximum of 1 only when all the alignment criteria are satisfied.

We now wish to incorporate this structural factor into the Hamiltonian in such a manner as to ensure that at small  $x_{\text{Hb}}$ , the two interacting blocks are unlikely to form H-bond. A simple phenomenological way to proceed is to introduce a potential profile which has two parameters dynamically modulated by  $x_{\text{Hb}}$  with a fixed solvation energy  $E_{\text{sol}}$

$$\begin{aligned} U_{\text{Hb}}(r, x_{\text{Hb}}) = & \frac{A(x_{\text{Hb}})}{r^k} \left[ \frac{1}{4r^{3k}} - \left( \frac{1}{r_{\text{Hb}}^x k} + \frac{1}{(r_{\text{Hb}}^*)^k} + \frac{1}{(r_{\text{Hb}}^{\text{sol}})^k} \right) \frac{1}{3r^{2k}} \right. \\ & \left. + \left[ \left( \frac{1}{r_{\text{Hb}}^x k} + \frac{1}{(r_{\text{Hb}}^*)^k} \right) \frac{1}{(r_{\text{Hb}}^{\text{sol}})^k} + \frac{1}{(r_{\text{Hb}}^x r_{\text{Hb}}^*)^k} \right] \frac{1}{2r^k} - \frac{1}{(r_{\text{Hb}}^x r_{\text{Hb}}^* r_{\text{Hb}}^{\text{sol}})^k} \right] \end{aligned} \quad (3)$$

Here the first dynamical parameter  $A(x_{\text{Hb}})$  is determined by fixing  $U_{\text{Hb}}(r_{\text{Hb}}^{\text{sol}}, x_{\text{Hb}}) = E_{\text{sol}}$  and for another parameter, we have used a linear relation  $r_{\text{Hb}}^x = x_{\text{Hb}} r_{\text{Hb}}^c + (1 - x_{\text{Hb}}) r_{\text{Hb}}^*$ . Examples of this modulated double-well profile are shown in fig.2(a). Note that even incorporated with this structural factor, the H-bond potential still remains pairwise between two interacting blocks.

Aside from the  $\text{NH} \cdots \text{OC}$  hydrogen bond, we include in our model the bonding between  $\text{C}_\alpha\text{-H} \cdots \text{O}=\text{C}^{27}$ . This interaction has a strong chirality<sup>22</sup> and an angular dependence that involves at least two contiguous blocks. From fig.1(d), we note that the native configuration for interacting, consecutive blocks  $i, i + 1$  and  $j, j + 1$  (here  $i(j) + 1$  is the block next to  $i(j)$  along the same strand) requires  $\widehat{\text{X}}_{23}^{(i)} \widehat{\text{X}}_{23}^{(j)}$  antiparallel to  $\widehat{\text{X}}_{23}^{(i+1)} \widehat{\text{X}}_{23}^{(j+1)}$ . Therefore, in analogy to the aforementioned H-bond, we propose a structural factor for this additional interaction

$$x_{\text{chiral}}^{(i,j)} = \frac{1}{4} x_{\text{Hb}}^{(i,j)} x_{\text{Hb}}^{(i+1,j+1)} \left[ 1 - \widehat{\text{X}}_{23}^{(i)} \cdot \widehat{\text{X}}_{23}^{(i+1)} \right] \left[ 1 - \widehat{\text{X}}_{23}^{(j)} \cdot \widehat{\text{X}}_{23}^{(j+1)} \right] \quad (4)$$

with an interaction potential  $U_{\text{C}_\alpha\text{H-OC}}(r, x_{\text{chiral}})$  taken to be similar to  $U_{\text{Hb}}(r, x_{\text{Hb}})$ . We use a  $\text{C}_\alpha\text{-H} \cdots \text{O}=\text{C}$  interaction strength half that of a single H-bond<sup>27</sup>.

### E. The role of the force field

To characterize the roles of structural factors and solvation effects in  $\beta$ -sheet formation, we have studied four different forms of the H-bond potential. These are:

- **(A) LJ<sup>fix</sup>**:  $U_{\text{LJ}}^{\text{fix}}(r) = |E_{\text{Hb}}| \frac{(r_{\text{Hb}}^c)^6}{r^6} \left[ \frac{(r_{\text{Hb}}^c)^6}{r^6} - 2 \right]$ , a L-J potential without angular dependence.

- **(B) Sol<sup>fix</sup>**:  $U_{\text{Sol}}^{\text{fix}}(r) \Rightarrow \text{eqn.}(1)$ , a double-well solvation potential without angular dependence.
- **(C) LJ<sup>ang</sup>**:  $U_{\text{LJ}}^{\text{ang}}(r) = A_{\text{LJ}}(x_{\text{Hb}}) \frac{[r_{\text{LJ}}(x_{\text{Hb}})]^6}{r^6} \left[ \frac{[r_{\text{LJ}}(x_{\text{Hb}})]^6}{r^6} - 2 \right]$ , a 2-dynamical-parameter L-J potential with our proposed angular dependence. This profile is designed to help distinguish the effects of solvation and structural factors. Thus, except for the absence of a desolvation barrier, this potential is quite similar to the solvation one, eqn.(3). Explicitly, we let a non-native alignment factor  $x_{\text{Hb}} < 1$  give rise to a linear shift  $|U_{\text{LJ}}^{\text{ang}}(r_{\text{LJ}}(x_{\text{Hb}}))| = A_{\text{LJ}}(x_{\text{Hb}}) = x_{\text{Hb}}|E_{\text{Hb}}| + (1 - x_{\text{Hb}})|E^{\text{sol}}|$  for the first parameter. Also, to achieve a repulsive effect similar to that in eqn.(3), we set  $U_{\text{LJ}}^{\text{ang}}(r_{\text{Hb}}^x) = U_{\text{Hb}}(r_{\text{Hb}}^x, x_{\text{Hb}})$ , i.e.,  $r_{\text{LJ}}(x_{\text{Hb}}) = r_{\text{Hb}}^x (1 + \sqrt{1 + U_{\text{Hb}}(r_{\text{Hb}}^x, x_{\text{Hb}})/A_{\text{LJ}}(x_{\text{Hb}})})^{1/6}$  for the second parameter. Fig.2(b) shows the modulation of this force field due to varying of structural factor.
- **(D) Sol<sup>ang</sup>**:  $U_{\text{Sol}}^{\text{ang}}(r) \Rightarrow \text{eqn.}(3)$ , the de/solvation potential with the proposed angular dependence, which constitutes our full model.

## F. The replica-exchange and Multi-canonical Technique

Throughout the entire paper, the simulation procedure employed a modified Verlet-Langevin algorithm. Specifically, for a particular set of coordinate  $\vec{x}(t)$  with velocity  $\vec{v}(t)$  and force  $\vec{f}(t)$ , the update at time  $t$ ,  $\Delta\vec{x}(t) \equiv \vec{x}(t + \Delta t) - \vec{x}(t)$  is obtained by

$$\begin{aligned}
\vec{x}(t \pm \Delta t) &= \vec{x}(t) \pm \vec{v}\Delta t + \frac{\Delta t^2}{2m} \vec{f} + O(\Delta t^3) \\
\vec{x}(t + \Delta t) - \vec{x}(t - \Delta t) &= 2\vec{v}(t)\Delta t + O(\Delta t^3) \\
\vec{x}(t + \Delta t) + \vec{x}(t - \Delta t) &= 2\vec{x}(t) + \frac{\Delta t^2}{m} \vec{f}(t) + O(\Delta t^4) \\
&= 2\vec{x}(t) + \frac{\Delta t^2}{m} \left[ -\zeta\vec{v}(t) - \vec{\nabla}_x E + \eta(t) \right] + O(\Delta t^4) \\
\Rightarrow \Delta\vec{x}(t) &= \left[ \frac{1 - \frac{\zeta\Delta t}{2m}}{1 + \frac{\zeta\Delta t}{2m}} \right] \Delta\vec{x}(t - \Delta t) + \frac{\Delta t^2 \left[ -\vec{\nabla}_x E + \eta(t) \right]}{m + \zeta\Delta t/2} + O(\Delta t^4) \quad (5)
\end{aligned}$$

with  $m$ ,  $\zeta$ ,  $E \equiv H(\{\vec{x}\})$ ,  $\eta$  as mass, viscosity, energy (Hamiltonian), and uncorrelated thermal noise, respectively, where  $\{\vec{x}\}$  represents the set of coordinates for entire system. Since the coordinates used in our simulations represent  $C_\alpha$  co-planes, the mass  $m$  and the radius for



viscosity  $\zeta$  are approximated from the mass of a single glutamine and the  $C_\alpha$  bond length, respectively.

The replica-exchange method<sup>20</sup> and multi-canonical rescaling technique<sup>21</sup> are used to obtain the density of states  $n(E)$  and hence thermodynamic properties of any given system. First, several simulations are performed at different temperatures. To enhance the sampling, configurations obtained at different temperatures  $T, T'$  were switched in between based on the Metropolis criterion<sup>20</sup> that obeys detail balance,

$$P\left(\left[\{\vec{x}\}_T, \{\vec{x}'\}_{T'}\right] \rightarrow \left[\{\vec{x}'\}_T, \{\vec{x}\}_{T'}\right]\right) = \begin{cases} 1 & \text{if } \Delta \leq 0, \\ e^{-\Delta} & \text{if } \Delta > 0. \end{cases} \quad (6)$$

with  $\Delta = [1/T - 1/T'] [E(\{\vec{x}'\}) - E(\{\vec{x}\})]$  (see Ref. 20 and references therein for more details). Second, an initial guess of  $n(E)$  is obtained by using a WHAM (weighted histogram analysis method)-like procedure<sup>14,20</sup>,

$$P_\beta(E) = \frac{n(E)e^{-\beta E}}{\sum_E n(E)e^{-\beta E}} \\ \Rightarrow n(E) \propto \left[ \sum_\beta \frac{e^{-\beta E}}{P_\beta(E)} \right]^{-1} \quad (7)$$

where  $\beta = 1/k_B T$  ( $k_B$  is Boltzmann factor) and  $P_\beta(E)$  is the probability of energy distribution accumulated from simulations at temperature  $T = 1/k_B \beta$ .

Then, we performed multi-canonical rescaling simulations to refine  $n(E)$ , in which we used the same Hamiltonian but the forces in equation of motion (5) were rescaled as  $\vec{\nabla}E \rightarrow \frac{\partial E'(E,T)}{\partial E} \vec{\nabla}E$  with  $E'(E,T)$  as a trial function. This rescaling will yield a probability distribution  $P_\beta(E) \propto n(E)e^{-\beta E'(E,T)}$ ; thus, if we choose  $E'(E,T) \sim k_B T \ln n(E)$ ,  $P_\beta(E)$  will become relatively flat and hence the sampling become more accurate (see<sup>21</sup> and reference therein for detailed discussion). Finally, the refined  $n(E)$  is obtained iteratively,

$$n(E)_i \propto \left[ \sum_\beta \frac{e^{-\beta E'(E,1/\beta)_i}}{P_\beta(E)_i} \right]^{-1} = \left[ \sum_\beta \frac{e^{-\ln n(E)_{(i-1)}}}{P_\beta(E)_i} \right]^{-1} = \frac{n(E)_{(i-1)}}{\sum_\beta [P_\beta(E)_i]^{-1}} \quad (8)$$

where  $i$  indexes the iterations.

## G. The local melting approach

Aside from examining the global cooperativity, we have also explored the thermodynamics of local binding events in the model system. The idea is that in the absence of

hydrophobic clustering, the system cooperativity (if any) must arise from a scaling up of small scale bound structures. In other words, folding of a specific part of the overall structure will be aided by any contiguous folded regions<sup>28</sup>; this can be investigated by exploring the conditional probabilities of residues of being folded (i.e., in their native position and orientation) or unfolded depending on whether their neighbors are folded or unfolded (i.e., the contact correlations). Specifically, we investigated two cases; the ensemble that has all blocks retained in their folded configurations aside from either a) a few blocks at the end of one  $\beta$ -strand or b) a few blocks buried inside the sheet.

To study these local sub-structures, we have assumed here that their thermodynamics will not be affected significantly by the dynamics of very distant blocks. This allows us to compute a “conditional” partition function in which, except for those specified blocks, the rest can be treated as frozen in their native positions. Doing this, the number of degrees of freedom is significantly reduced and the conditional partition function can be obtained by explicit numerical integration. For instance, in the single-block  $\beta$ -tail case, the partition function reads  $\int dX_2 dX_3 \delta(\overline{X_1 X_2} - \overline{X_1 X_2}^N) \delta(\overline{X_2 X_3} - \overline{X_2 X_3}^N) e^{-H/k_B T}$  where  $\overline{X_1 X_2}^N = 3.75 \text{ \AA}$ ,  $\overline{X_2 X_3}^N = 0.57 \text{ \AA}$  are native constants, and  $X_2, X_3$  are the virtual points of the movable terminal block (note that its  $X_1$  is fixed). Then, because of the  $\delta$  functions, the partition function is reduced to an integral over three angles defining the orientation of the terminal plane.

### III. RESULTS

#### A. Global Cooperativity

The first system we studied is a 3-strand  $\beta$ -sheet with a total of 6 H-bonds equally distributed between adjacent strands. Since there is no sequence specificity, we artificially tethered the H-bonds at the 2 expected turns to maintain the  $\beta$ -sheet propensity. In Fig. 3, we show the computed specific heat for the four different model forces. Basically, we found that there is no sharp transition for the three models  $LJ^{fix}$ ,  $LJ^{ang}$ ,  $Sol^{fix}$  if non-specific H-bonds are allowed to develop on the peptide backbone; this is because their dominant low-energy states are ensembles with non-specific, randomly collapsed structures rather than a uniquely defined  $\beta$ -sheet (similar to the results observed by Guo & Brooks<sup>14</sup>). The complete

model  $\text{Sol}^{ang}$ , however, can define a unique native state and give rise to a sharp transition, as seen in Fig. 3(a).

Next, we added a  $\text{G}\bar{o}$ -like restriction to the models  $\text{LJ}^{fix}$ ,  $\text{LJ}^{ang}$ ,  $\text{Sol}^{fix}$ , i.e., allowing H-bond formation only between those residues that have such an interaction in the native  $\beta$ -sheet structure<sup>10</sup>. Of course, the entire justification of this approach is absent in systems with homogeneous interaction as the one of primary concern here, but it is still worthwhile comparing the results of our proposed complete model with these alternatives. Note however that our  $\text{G}\bar{o}$ -like restriction does not include any additional restrictions on backbone configurations to favor a particular structure (i.e., native state); this is very different from the energetic restrictions commonly used in the off-lattice protein folding literature<sup>11</sup>. In Fig. 3(b), we show that even with  $\text{G}\bar{o}$ -like restrictions to reduce the non-specific collapsed ensemble, the  $\text{LJ}^{fix}$  model can not give rise to a sharp transition compared with models incorporating either the de/solvation effect or angular dependency. This is consistent with results from other group<sup>13</sup> and also the aforementioned reasoning that with only two contact couplings for each interacting unit, a simple force field for H-bond formation can not produce systemic cooperativity.

The difference between the various force models becomes much clearer in larger systems. Fig. 3(c) shows the specific heat diagrams for a 4-strand  $\beta$ -sheet with a total of 15 H-bonds equally distributed between adjacent strands. Now, without a significant increase in the transition temperature, the peak magnitude of the specific heat for model  $\text{Sol}^{ang}$  is 100 fold larger than that of the previous small system, whereas there is still no significant transition for the L-J  $\text{G}\bar{o}$ -like potential. This difference is further realized by examining the density of states. In Fig. 4(a), we note that there is only one dominant ensemble for model  $\text{LJ}^{fix}$  in the low-energy region; this ensemble mixes the native and partially folded states. In model  $\text{LJ}^{ang}$ , on the other hand, the unfolded ensemble ( $E \sim 0$ ) is slightly separated from the folded one; however, the folded phase has a larger entropy than that of the unfolded state, and thus there is no transition. In the solvation model, as shown in Fig. 4(b), there is a clear separation between the folded and unfolded ensemble, with the unfolded states having the largest entropy, as is crucial for having a sharp transition.

Apparently, both the angular dependence and solvation effect slightly enhance the system cooperativity, but only a combination of both can yield the desired results in the system of primary concern here. This point has not been adequately addressed in previous works<sup>13,14</sup>.

Also, we notice a high energy population appearing in model  $LJ^{ang}$ ,  $Sol^{fix}$ , and  $Sol^{ang}$ . Analyzing the contact profile in this additional phase, we found that its dominant configurations are those with significant intervening of folding and unfolding in the entire structure, i.e., “droplet”-like structures<sup>28,29</sup>. As will be elucidated in next section, this intervening can lead to an interfacial energetic penalty resulting from backbone twisting (enhanced by the angular dependence) and (re)-desolvation barrier crossing at the interface between contiguous folded and unfolded regions; thus the partially unfolded ensemble is shifted from low energy (as in model  $LJ^{fix}$ ) to the high energy region. Consequently, the completely folded and unfolded ensemble are well separated, leading to a sharp transition.

Of course, whether these partially folded droplet configurations can be shifted to high energy depends not only on the choice of the H-bond potential (to create the interfacial penalty), but also the topology of the  $\beta$ -sheet. When the H-bond energy inside the folded droplet can compensate the interfacial penalty, the structure will no longer stay at high-energy phase. To show this explicitly, we studied a system that is less symmetric on the  $\beta$ -sheet plane; we chose a 3-strand  $\beta$ -sheet with long strands, looking at the effect of increasing the strand length. We started with a 3-strand  $\beta$ -sheet with a total of 30 H-bonds equally distributed between adjacent strands. Fig. 5(a,b) shows its  $n(E)$  and specific heat, which are very similar to those of the 4-strand, 15 H-bond system, in that they both have well-separated unfolded/native states, and partially unfolded high-energy populations. Analyzing the states in the low and high energy partially folded ensembles, we found that their dominant configurations are droplets with one (in the low energy phase) or multiple (in the high energy phase) interfaces between contiguous un/folded regions, i.e., a partially folded  $\beta$ -sheet (or hairpin) buried in unfolded coils (illustrated by examples in Fig. 5(a)).

When the system size increases to a total of 40 H-bonds, however, (see Fig.6(a,b)), we find an increased weight for the partially folded ensemble in the low energy phase ranging from  $0 > E > E_N$  where  $E_N$  is the native state energy. Unlike the smaller, or symmetric system, here the interfacial energy penalty between contiguous un/folded regions, can not compete with the large H-bond energy at the bulky folded portion; this allows the partially folded ensemble to have a low energy. Moreover, in a system with such an elongated asymmetry, the partially folded portion can freely move along the  $\beta$ -sheet, or freely slide along the chain with many “mis-pairing” H-bonds (i.e., inconsistent with native pairing). Both effects can then increase the entropy of the partially folded (or even misfolded) ensemble and hence smears

out the separation between completely un/folded ensemble and partially folded ensemble, Fig. 6(a). The smearing becomes more significant in a larger 3-strand  $\beta$ -sheet with a total of 50 H-bonds, Fig. 6(c). As a consequence, the system becomes less cooperative and an additional continuous transition occurs between these partially un/folded ensemble, fig.6(b,c). Developing a phenomenological model based on these results to study how the system cooperativity depends on the  $\beta$ -sheet topology, therefore, is one of our future goals.

### B. Local Bonding Effects

In this section, we examine how the model system acquires “global” cooperativity (in the absence of hydrophobic clustering) by exploring the thermodynamic effects of local un/bonding. Here, since we are dealing with only a small number of degrees of freedom, we could calculate all thermodynamic properties by explicit integration of the partition function. As an illustration, we first present the results of the single-block  $\beta$ -tail case, Fig. 7, where we plotted the probability distribution function (pdf)  $P(r)$  of the interacting distance  $r$  in the native NH $\cdots$ OC pair between the terminal block (the one allowed to fluctuate) and its native partner (taken to be frozen in space).

In this case, the maximum possible NH $\cdots$ OC distance as determined by the range of integration, is smaller than that necessary to fit a water molecule in between and thus there cannot be any true secondary solvated minimum. We do see however the fact that having the solvation barrier and (to a lesser extent) the angular factors make a big difference in the structure of  $P(r)$ . Specifically, there is no hint of well-separated 2-state behavior for model LJ<sup>fix</sup>. However, a small barrier appears if the potential has an angular dependence (model LJ<sup>ang</sup>), and becomes significant if solvation effects are included (model Sol<sup>fix</sup>, Sol<sup>ang</sup>). Here, we note that because of the bond angle  $\angle C' C_\alpha N$  potential,  $P(r)$  is concentrated on the “ring” that satisfies  $\angle C' C_\alpha N = \angle C' C_\alpha N_{\text{native}}$ . On this ring, only a few “points” will give minimal dihedral angle ( $\psi, \phi$ ) energies. These points correspond to the sharp peaks in fig.7 that have free energy difference  $\approx \epsilon_\psi + \epsilon_\phi \approx 1\text{kcal/mol}$  from their surrounding; if we reduce the bond angle stiffness  $k_\theta$ , these sharp peaks become broadened (data not shown). Apparently, this effect comes from the backbone energy and is independent of the choice of H-bond potential.

Next, we studied the “buried” cases with  $n$  blocks allowed to fluctuate. In this situation,

the configurations of fluctuating blocks are clearly constrained to a great extent by their fixed neighbors. Thus, we found that for  $n = 1$ , there is neither 2-state behavior nor any qualitative difference among the results of different force fields (data not shown); all significant probability is confined in the H-bond well, indicating a strong topological confinement to force the folding of a single unfolded block buried amidst folded ones. When  $n = 2$ , we still do not have enough freedom of backbone motion to allow for a solvated second minimum for the main H-bond; the maximum separation is slightly above  $4.1 \text{ \AA}$ , Fig. 8(a). Nonetheless, we see clear differences among different models. For the simplest  $\text{LJ}^{fix}$  model, there is no confinement to a narrow contact well. Adding the angular factor back in, we create a barrier as the  $\text{NH} \cdots \text{OC}$  distance is increased. This barrier is due to the modulation of the LJ potential by the angular factor, making it repulsive if the orientation is not properly matched. Alternatively, adding the solvation effect as in model  $\text{Sol}^{fix}$  also introduces a barrier; this is because rolling of the co-plane allows for a wide separation (and hence going up and down the solvation barrier) in the  $\text{C}_\alpha\text{H} \cdots \text{OC}$  interactions. Finally, putting both effects in leads to a very large degree of confinement in the H-bond well, suggesting that local coupling is enhanced by both structural and solvation effects such that an unfolded block is strongly biased to fold if contiguous to folded ones.

To further characterize the difference between the varying choices of force models, we explored the un/folding correlation in the 2-block buried case. Specifically, we computed the conditional probability function  $P(r)$  for one block with respect to the un/folding state of another (defined as folded/unfolded if its native H-bond separation  $r_2 \gtrless r_{\text{Hb}}^*$ ),  $P(r_1|r_2 > r_{\text{Hb}}^*)$ ,  $P(r_1|r_2 < r_{\text{Hb}}^*)$ , where  $r_1, r_2$  are their native H-bond separations, respectively. In other words, if the system has a good local coupling, un/folding of one block should force the un/folding of another, implying a well-separated  $P(r_1|r_2 \gtrless r_{\text{Hb}}^*)$ . In Fig. 8(b), however, we found that  $P(r_1|r_2 \gtrless r_{\text{Hb}}^*)$  are well separated only in model  $\text{Sol}^{ang}$ . Here, the separated probability distributions have been individually normalized; the actual probability for being at the larger  $r$  is extremely small as is evident from Fig. 8(a). Also, note that it is not  $r$  in the figure which is important - this H-bond separation is quite small. Instead, the two peaks correspond to either having the full H-bond energy (by satisfying *both* the distance and angular conditions) or not having that energy; the distribution at larger  $r$  does not have the correct angular configuration. To clarify this point, we plotted the conditional probability function on the variation of H-bond energy  $E$  instead of distance  $r$ , i.e.,  $P(E_1(r_1)|r_2 >$

$r_{\text{Hb}}^*$ ),  $P(E_1(r_1)|r_2 < r_{\text{Hb}}^*)$ , Fig. 8(b). Now, we see clearly that only the full model  $\text{Sol}^{\text{ang}}$  has a significant separation effect.

### C. Collective Re-solvation Kinetics

The conclusion from the local coupling studies is that the full model being proposed here leads to strong correlations between the behaviors of neighboring blocks. For the system as a whole, this should mean that complicated configurations with repeated interfaces between unfolded and folded residues would cause additional energetic penalties and thus can be strongly suppressed in favor of simpler configurations with large patches of residues being either all in contact or all not in contact. Of course, whether the system can therefore acquire an global cooperativity would depend on its topology as well, as revealed in earlier section.

Now, the interesting part of this conclusion, as will be illustrated later, is that during unfolding (folding), the solvation (desolvation) process must occur in a collective way. To see this explicitly, we show the pdf and re-solvation kinetics of a 10-block buried case in Fig. 9(a,b). Because of the large barrier needed to melt the blocks, here we set the simulation temperature far beyond the physiological range.

From Fig. 9(a) (using  $\text{Sol}^{\text{ang}}$ ), we note that the pdf of native H-bond distances are well separated by a free energy ( $-k_B T \ln P(r)$ ) barrier, resulting in an ordered (H-bond formed) and disordered (H-bond not formed) phases. Interestingly, even governed by the same force law, the un/folding barriers for the various molten blocks are not quite the same. For blocks close to the confined ones (those frozen in the space), the barrier progressively increases, and the disordered phase becomes less significant. This reduction of disordered phase manifests a stronger folding bias for any unfolded residues near those folded ones. Thus it is not effective to unbind the blocks one by one, since the unbound block will rebind long before its neighbor has unbound. This can be seen in the high-temperature unfolding simulation, Fig. 9(b), in which we note that the resolvation (i.e., infiltration of water molecules) process involved many residues simultaneously. In Fig. 9(c), we show that this collective water infiltration indeed occurs in unfolding of the entire  $\beta$ -sheet.

#### IV. DISCUSSION

We have explored the mechanism of  $\beta$ -sheet cooperativity without side-chain interactions, with different choices of the H-bond potential. Our results suggest that in the absence of hydrophobic clustering, the  $\beta$ -sheet cooperativity arises from a coupling of structural factor (contact angular dependence), protein de/solvation effects, and the system topology. Since this phenomenon is sequence-independent, the results can be considered to apply in general to  $\beta$ -sheet structures.

Given the coupling number for each H-bond interacting unit, our results differ from most 2-dimensional pairwise-interacting system, in that there the minimal number of coupling required for global cooperativity is larger than the one present here. Thus, the coupling between backbone energy (the angular dependence) and pairwise H-bond interaction (incorporated with solvation dynamics) must yield a strong many-body effect, which has been argued to be crucial to produce systemic cooperativity in homogeneous system such as are the primary concern here<sup>28</sup>. Apparently, our model system has a default many-body effect, the dihedral confinement via the corresponding terms in the backbone energy.

As illustrated in our study, when the system is close to the fully folded state, the dihedral confinement is strong enough to complete the folding (the  $n = 1$ -block case). However, it is too weak to confine the backbone collectively if there is a larger unfolded portion in the  $\beta$ -sheet, as illustrated in the pure Lennard-Jones potential case. Instead, it is the angular dependence which incorporates the contact strength into the backbone Hamiltonian and thus amplifies the confinement. This leads to a competition with solvation dynamics; in other words, while the solvent tries to pull the interacting blocks apart, the confining force amplified by folded neighbors can hold them back. As this behavior occurs mainly between contiguous un/folded regions, it creates an “interfacial” energetic penalty and the “droplet” picture proposed in previous works<sup>28,29</sup> (now allowing a measurement the droplet surface tension). Consequently, in a partially folded structure, any small regions of unfolded blocks contiguous to folded ones are thermodynamically unfavorable and will be forced to fold or will unfold the folded ones<sup>28</sup>. Thus, while there has been a concentration of effort on understanding the role the sequence heterogeneity for protein folding and design, we would like to point out that this generic cooperativity buried in the  $\beta$ -sheet architecture can also serve as a *building block* to construct macromolecular structure. However, this same building



block can also provides the mechanism for pathological aggregation.

What then would be the physiological role and evolutionary principle of having sequence heterogeneity, in the presence of possible  $\beta$ -architectures? Certainly, with the fast time scale (of order of 0.1 ns, estimated from our Langevin simulations) for a single  $C_\alpha$  block folding, any pre-folded  $\beta$ -architecture with ordered, exposed amide and carbonyl oxygen could lead to a seeding process and non-specifically precipitate surrounding unfolded peptides; this has been observed in the elongation process of amyloidogenesis<sup>3</sup>. The physiological role of heterogeneity, therefore, would be to either distort the orientation of exposed amide and carbonyl groups into a non-aggregation competent form, or provide “hot” nuclei to bias the system into the native fold. Indeed, this idea has been verified in a recent tryptophan zipper model<sup>30</sup>. Exploring the competition between native folding due to specific sequence heterogeneity and pathological aggregation due to generic cooperativity is perhaps the most important direction for future study.

As a side point, to elucidate the effect of local un/binding, we have introduced a local melting method. This method can be further used to explore local nucleation or de-solvation events in any system lacking long-ranged spatial couplings. Also, instead of simulating all backbone atoms or a simplified  $C_\alpha$  model, a functional block (co-plane) approach was proposed. This approach greatly reduces our computational effort; however, it still keeps the right angular degrees of freedom (missing in  $C_\alpha$  model) and gives rise to a structural factor (i.e., backbone alignment) that helps account for  $\beta$ -sheet cooperativity.

Also, we have introduced an approach to de/solvation which can be used directly for Langevin simulations. It has been noticed that the (de)-solvation effects are important in protein folding and functioning, but no standard model has been proposed<sup>15,16,17,18,19,23,24,25</sup>. Also, we note that solvent dynamics can be regulated by system hydrostatic pressure<sup>15</sup>. Interestingly, many adhesion and hemostasis-related proteins are very sensitive to shear stress and pressure change; perhaps a local de/re-solvation event might trigger a cooperative conformational change which ultimately has large scale consequences<sup>19</sup>. Thus, microscopic cooperativity can be amplified into a macroscopic response; this also needs to be explored in future work.

## V. ACKNOWLEDGEMENT

CG wishes to acknowledge Peter G. Wolynes, Jose N. Onuchic, Angel E. Garcia, Tobin R. Sosnick, Joan-Emma Shea, and Ken A. Dill for comments the solvation model, and Christopher M. Dobson for comments on sequence-independent mechanism. He also thanks to A.E. Garcia for a careful reading on the manuscript.

- 
- <sup>1</sup> M. Sunde, L.C. Serpell, M. Bartlam, P.E. Fraser, M.B. Pepys, and C.C. Blake, *J. Mol. Biol.* **273**, 729 (1997).
  - <sup>2</sup> K. Liu, H.S. Cho, H.A. Lashuel, J.W. Kelly, and D.E. Wemmer, *Nat. Struc. Biol.* **7**, 754 (2000).
  - <sup>3</sup> J.W. Kelly, *Nat. Struc. Biol.* **7**, 824 (2000).
  - <sup>4</sup> A. Fersht, in *Structure and mechanism in protein science*. (W.H. Freeman & Company. New York, 1999) Chapter 17.
  - <sup>5</sup> M.F. Perutz and A.H. Windle, *Nature* **412**, 143 (2001). M.F. Perutz, T. Johnson, M. Suzuki, and J.T. Finch, *Proc. Natl. Acad. Sci. USA.* **91**, 5355 (1994).
  - <sup>6</sup> S. Koide, X. Huang, K. Link, A. Koide, Z. Bu, and D.M. Engelman, *Nature* **403**, 456 (2000).
  - <sup>7</sup> M. Fändrich, M.A. Fletcher, and C.M. Dobson, *Nature* **410**, 169 (2001).
  - <sup>8</sup> T. Kortemme, M. Ramirez-Alvarado, and L. Serrano, *Science* **281**, 253 (1998).
  - <sup>9</sup> N.V. Dokholyan, S.V. Buldyrev, H.E. Stanley, and E.I. Shakhnovich, *J. Mol. Biol.* **296**, 1183 (2000).
  - <sup>10</sup> Y. Ueda, H. Taketomi, and N. Gō, *Biopolymers* **17**, 1531 (1978).
  - <sup>11</sup> C. Clementi, H. Nymeyer, and J.N. Onuchic. *J. Mol. Biol.* **298**, 937 (2000).
  - <sup>12</sup> R.K. Pathria, *Statistical Mechanics* (Butterworth Heinemann, Oxford, 1996), Chapter. 12.
  - <sup>13</sup> G.F. Berriz, A.M. Gutin, and E.I. Shkhnovich, *J. Chem. Phys.* **106**, 9276 (1997).
  - <sup>14</sup> Z. Guo and C.L. Brooks, *Biopolymers*, **42**, 745 (1997).
  - <sup>15</sup> G. Hummer, S. Garde, A.E. Garcia, M.E. Paulaitis, and L.R. Pratt, *Proc. Natl. Acad. Sci. USA.* **95**, 1552 (1998).
  - <sup>16</sup> A.E. Garcia and G. Hummer, *Protein: Structure, Function, & Genetics.* **38**, 261 (2000).
  - <sup>17</sup> J.D. Dunitz, *Science* **264**, 670 (1997).
  - <sup>18</sup> H.S. Ashbaugh, E.W. Kaler, and M.E. Paulaitis, *J. Am. Chem. Soc.* **121**, 9243 (1999).

- <sup>19</sup> R. Celikel, Z.M. Ruggeri, and K.I. Varughese, K.I. Nat. Struc. Biol. **7**, 881 (2000); P. Marchese, E. Saldivar, J. Ware, and Z.M. Ruggeri, Z.M. Proc. Natl. Acad. Sci. USA. **96**, 7837 (1999).
- <sup>20</sup> Y. Sugita, A. Kitao, and Y. Okamoto, J. Chem. Phys. **113**, 6042 (2000).
- <sup>21</sup> U.H.E. Hansmann, Y. Okamoto, and F. Eisenmenger, Chem. Phys. Lett. **259**, 321 (1996).
- <sup>22</sup> S. Takada, Z. Luthey-Schulten, and P.G. Wolynes, J. Chem. Phys. **110**, 11616 (1999).
- <sup>23</sup> N. Helson, J.N. Onuchic, and A.E. Garcia, Proc. Natl. Acad. Sci. USA. **96**, 14848 (1999).
- <sup>24</sup> B. Roux, and T. Simonson, Biophys. Chem. **78**, 1 (1999).
- <sup>25</sup> Head-Gordon, T., Stillinger, F.H. J. Chem. Phys. **98**, 3313 (1993).
- <sup>26</sup> T.E. Creighton, in *Proteins: structure and molecular properties* (W.H. Freeman and Company. New York. 1996) Chapter 4 & 5.
- <sup>27</sup> R. Vargas, J. Garza, D.A. Dixon, B.P. Hay, J. Am. Chem. Soc. **122**, 4750 (2000).
- <sup>28</sup> C. Guo, H. Levine, and D.A. Kessler, Phys. Rev. Lett. **84**, 3490 (2000); Proc. Natl. Acad. Sci. USA. **97**, 10775 (2000).
- <sup>29</sup> P.G. Wolynes, *Proc. Natl. Acad. Sci. USA* **94**, 6170 (1997).
- <sup>30</sup> A.G. Cochran, N.J. Skelton, and M.A. Starovasnik, Proc. Natl. Acad. Sci. USA **98**, 5578 (2001).

## VI. FIGURE CAPTIONS

**Fig.1** (a) The co-planar structure with (b) the three virtual points  $\{X_1, X_2, X_3\}$  and dihedral angles  $\omega, \phi, \psi$  labeled. The virtual bond lengths and angles are determined so as to give (c) a regular, symmetric  $\beta$ -sheet structure with side-chains and  $C_\alpha H$  bonds alternately pointing up and down periodically. (d) The side-chain and  $C_\alpha-H \cdots OC$  interactions are indicated by light-gray, gray arrows, respectively, with the shadowed area indicating the atoms involved determining the angular dependence of a single H-bond. (e) If two interacting blocks  $i, j$  are to have a native H-bond (the gray arrow), proper alignment of two pairs of planar vectors and collinearity of the two sets of points  $(X_1^{(i)}, X_2^{(j)}, X_3^{(j)}; X_1^{(j)}, X_3^{(i)}, X_2^{(i)})$  are required.

**Fig.2** The structural-factor-dependent H-bond potential profiles in units of kcal/mol with interaction distance  $r$  ( $NH \cdots OC$ ) measured in  $\text{\AA}$ . (a) The (de)-solvation force field  $U_{Hb}(r, x_{Hb})$ . The barrier height between  $r = r_{Hb}^*$  and the solvent-separated minimum ( $r = r_{Hb}^{sol}$ ) represents the free energy cost in desolvation cavity formation. Here we have graphed  $U_{Hb}(r, x_{Hb})$  from  $x_{Hb} = 0$  to 1. The dashed curve represents the modulation of the contact minimum ( $r_{Hb}^x, U_{Hb}(r_{Hb}^x, x_{Hb})$ ). (b) The Lennard-Jones force field  $U_{LJ}^{ang}(r)$ , where the profile is modulated by changing the contact minimum (long-dashed curve)  $|U_{LJ}^{ang}(r_{LJ}(x_{Hb}))| = x_{Hb}|E_{Hb}| + (1 - x_{Hb})|E^{sol}|$  from the H-bond contact energy  $E_{Hb}$  to the single  $H_2O$  hydration  $E^{sol}$ . The major difference between (a) and (b) is the desolvation barrier.

**Fig.3** (a) The specific heat for a 3-strand with 6 H-bonds modeled by different force fields (without  $G\bar{o}$ -like restrictions). Here, because of the absence of  $G\bar{o}$ -like pairing, the three force field  $LJ^{fix}$ ,  $LJ^{ang}$ , and  $Sol^{fix}$  are unable to define a unique structure and hence there is no obvious peak (i.e., transition) in their CV diagrams. Whereas force field  $Sol^{ang}$  can define unique  $\beta$ -sheet and hence leads to a sharper transition. (b) Same as (a) except for the  $G\bar{o}$ -like restrictions to model  $LJ^{fix}$ ,  $LJ^{ang}$ , and  $Sol^{fix}$  here. Note that the transitions for these three force fields become more apparent but still not compatible with  $Sol^{ang}$ . (c) The specific heat for a 4-strand with 15 H-bonds modeled by different force fields. Now the transition for  $Sol^{ang}$  become much stronger and there is almost no transition for L-J type force fields (inset).

**Fig.4** The density of state for a 4-strand  $\beta$ -sheet with 15 H-bonds. (a): The density of state for L-J type potential (with  $G\bar{o}$ -like restrictions). Note the distribution of entropy

and the high-energy population appearing in model LJ<sup>ang</sup>; this population contains partially folded state. **(b)**: The density of state for Sol type potential. Note that a good separation between the unfolded and folded ensemble only appeared in model Sol<sup>ang</sup>.

**Fig.5** The density of state **(a)**:  $n(E)$ , specific heat **(b)**  $C_v = \frac{\partial \langle E \rangle}{\partial T}$ , and energy  $\langle E \rangle$  (inset in **(b)**) for system asymmetrically elongated at one direction on its  $\beta$ -sheet plane (using model Sol<sup>ang</sup>). Here the system is a 3-strand  $\beta$ -sheet with total 30 H-bonds equally distributed between adjacent strands. Note the suppression of low-energy ensemble (between the completely unfolded and native states) and the appearance of high-energy population. The dominant configurations in these ensemble (insets) are “droplets” with interfaces between contiguous un/folded regions. Note that the low-energy configuration has less interface compared with high-energy one. The negative energy of the unfolded state comes from the two tethered  $\beta$ -turns.

**Fig.6 (a)**: The  $n(E)$  for a 3-strand  $\beta$ -sheet with total 40 H-bonds. Note the growth of partially folded ensemble (inset in **(a)** is a typical example of their configurations) at low-energy phase and smears out the separation between unfolded and the native states. This can lead to an abrupt transition (with the native state) at low temperature phase (pointed by double arrows in **(b)**) and a continuous transition (with other high-energy unfolded states) at high temperature phase (pointed by a single arrow in **(b)**). When the system size increases to totally 50 H-bonds **(c)**, the smearing becomes more significant (arrow in **(c)**) and the system eventually loses its cooperativity.

**Fig.7** The numerical results for the probability distribution function (pdf)  $P(r)$  of NH $\cdots$ OC separation  $r$  of the “molten” block respective to its native partner in the  $\beta$ -tail single-block case (indicated in the inserted diagram; black: frozen, gray: mobile). Here temperature: 25°C and integration step  $\delta\theta = 10^{-4}$ . Also, the curves have been adjusted up/downward for a better visual comparison. Note that the barrier for model Sol<sup>fix</sup> is much larger than that of Sol<sup>ang</sup>. This is because the desolvation barrier height is fixed in the former case, but modulated (by the angular factor) in the latter one.

**Fig.8** The numerical results for buried two-block cases. **(a)** The pdf  $P(r)$  for the native H-bond separation (average of the two symmetric mobile blocks). **(b)** The normalized conditional pdf in first molten block,  $P(r_1)$ , with respect to whether the second block is unfolded (defined as if  $r_2 \geq r_{\text{Hb}}^*$ ) or folded (defined as if  $r_2 < r_{\text{Hb}}^*$ ). Here  $r_1, r_2$  are the H-bond separations of the two molten blocks with their native partner, respectively, and

$\int dr_1 P(r_1 | r_2 \geq r_{\text{Hb}}^*) = 1$ . **(c)** The normalized conditional pdf in first molten block,  $P(E_1)$ , plotted on its H-bond energy  $E_1$ .

**Fig.9 (a):** Langevin simulation results of a ten-block buried case. Each curve represents the corresponding block in the inset diagram, averaged over the symmetrical pair. The simulation is averaged over 25 series of 1 ms runs ( $\Delta t = 5 \times 10^{-5}$  ps). **(b):** Snapshot of re-solvation simulation at  $T = 850^\circ\text{K}$  where each heavy atom is labeled by different symbols depending on the corresponding H-bond interacting distance  $r$ : “●” ( $r < r_{\text{Hb}}^*$ ), “○” ( $r_{\text{Hb}}^* \leq r < r_{\text{Hb}}^{\text{sol}}$ ), and “ ” ( $r \geq r_{\text{Hb}}^{\text{sol}}$ ). **(c):** Snapshot of unfolding simulation of a 4-strand  $\beta$ -sheet with 15 H-bonds at  $T = 800^\circ\text{K}$  where we have tethered the H-bond at the turn area to maintain the  $\beta$ -turn propensity. The time courses are plotted on the change of total H-bond (indicated by  $r \leq r_{\text{Hb}}^*$ ) number  $Q_{\text{Hb}}$  and energy  $E_{\text{Hb}}$  (kcal/mol), and configurations at different snapshots (a,b,c,d,e) are projected to left-hand side. Note the successive infiltration of water, and the overshoot of  $E_{\text{Hb}}$  at the abrupt transition point, manifesting a collective barrier crossing for the re-solvation process.

## APPENDIX A: MODIFIED DESOLVATION POTENTIAL

The simplified double-well potential provides the basic insight on how de/solvation effect involves in protein cooperativity. However, one might wish to modify this model to include more control parameters. For this purpose, we propose an alternative potential

$$U_{\text{HB}}(r) = \begin{cases} -B \frac{(r-r_1)^2 - h_1}{(r-r_1)^{2m+h_2}} & \text{if } r > r_{x1}, \\ Ay(r) \{ [y(r)]^2 + b \} + U_{\text{HB}}(r_{x1}) & \text{if } r \leq r_{x1} \\ \text{with } \begin{cases} y(r) = \frac{z(r)[z(r)-1]}{z(r)+s}, \\ z(r) = \frac{r_{x1}/r-1}{r_{x1}/r_{x0}-1} \end{cases} \end{cases}$$

and  $r$  as the distance between NH and CO, fig.1(a). Here, the interacting distance for formation of contact, desolvation barrier, and single-solvent separation are  $r = r_0$ ,  $r = r_1$ ,  $r = r_2$ , with free energy amplitude  $D_0$ ,  $D_1$ ,  $D_2$ , respectively, and the width of the contact well is controlled by the span between  $r = r_{x0}$  and  $r = r_{x1}$ . Normally,  $r_2$  is separated from  $r_0$  by the size of a single water molecule. The integer  $m > 2$ , on the other hand, is chosen for the long-distance behavior, and the six unknowns  $B, h_1, h_2, A, b, s$  can be determined by  $D_0, D_1, D_2, r_0, r_2$  and one continuity requirement ( $dU_{\text{HB}}/dr$  at  $r = r_{x1}$ ). Using this model,

one has a complete control on the potential profile (the well width for the contact entropy, e.g.).

To incorporate the fully Lennard-Jones behavior into the profile at both short ( $r \ll r_{\text{Hb}}^*$ ) and long ( $r \gg r_{\text{Hb}}^{\text{sol}}$ ) range region, we also proposed another force field

$$U_{\text{HB}}(r) = A \left( \frac{r_0}{r} \right)^6 \left[ \left( \frac{r_0}{r} \right)^6 - 2 \right] + \frac{Br^{6m}}{1 + Cr^{12m}}$$

with  $m$  as a positive integer and  $A, B, C > 0$ . Here the second term is designed to produce the desolvation granularity effect.

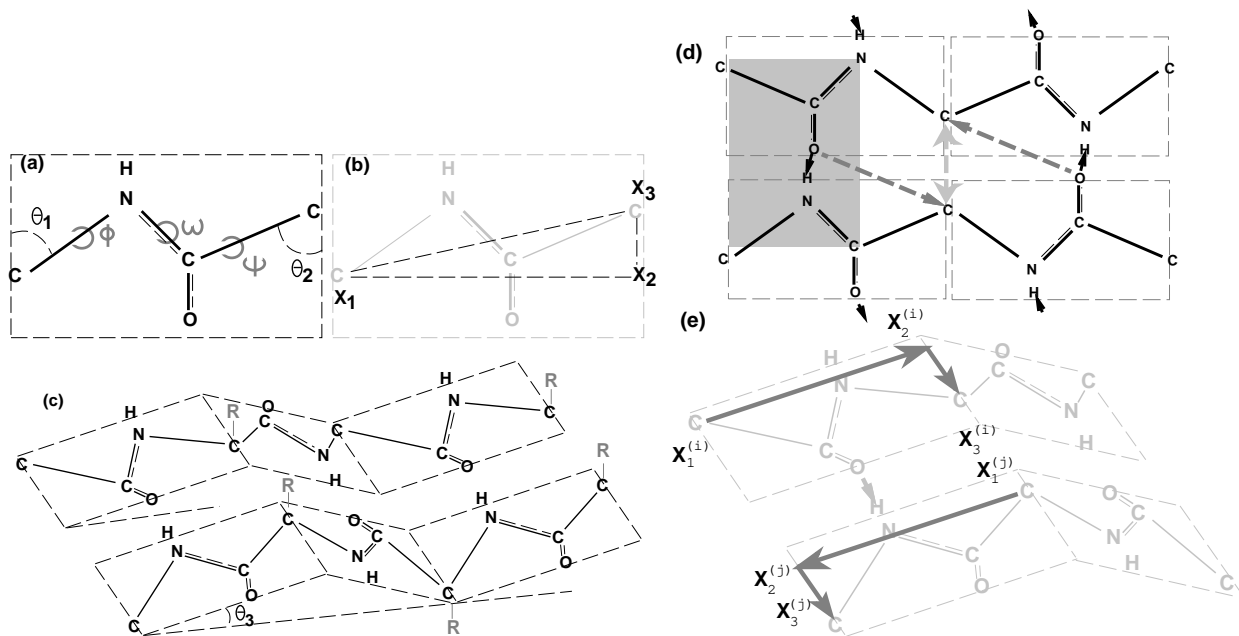


FIG. 1:

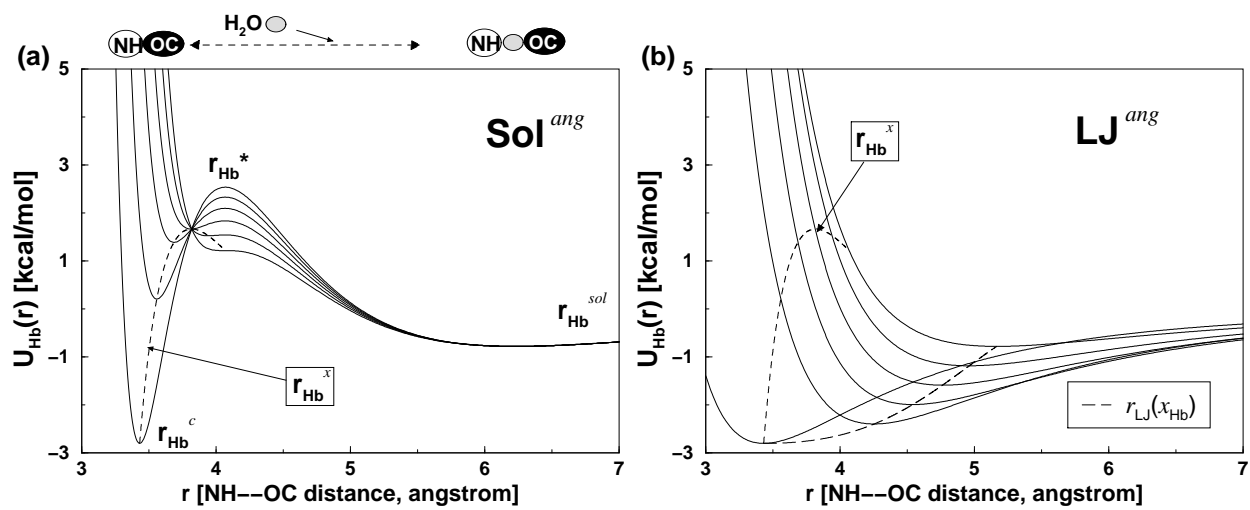


FIG. 2:



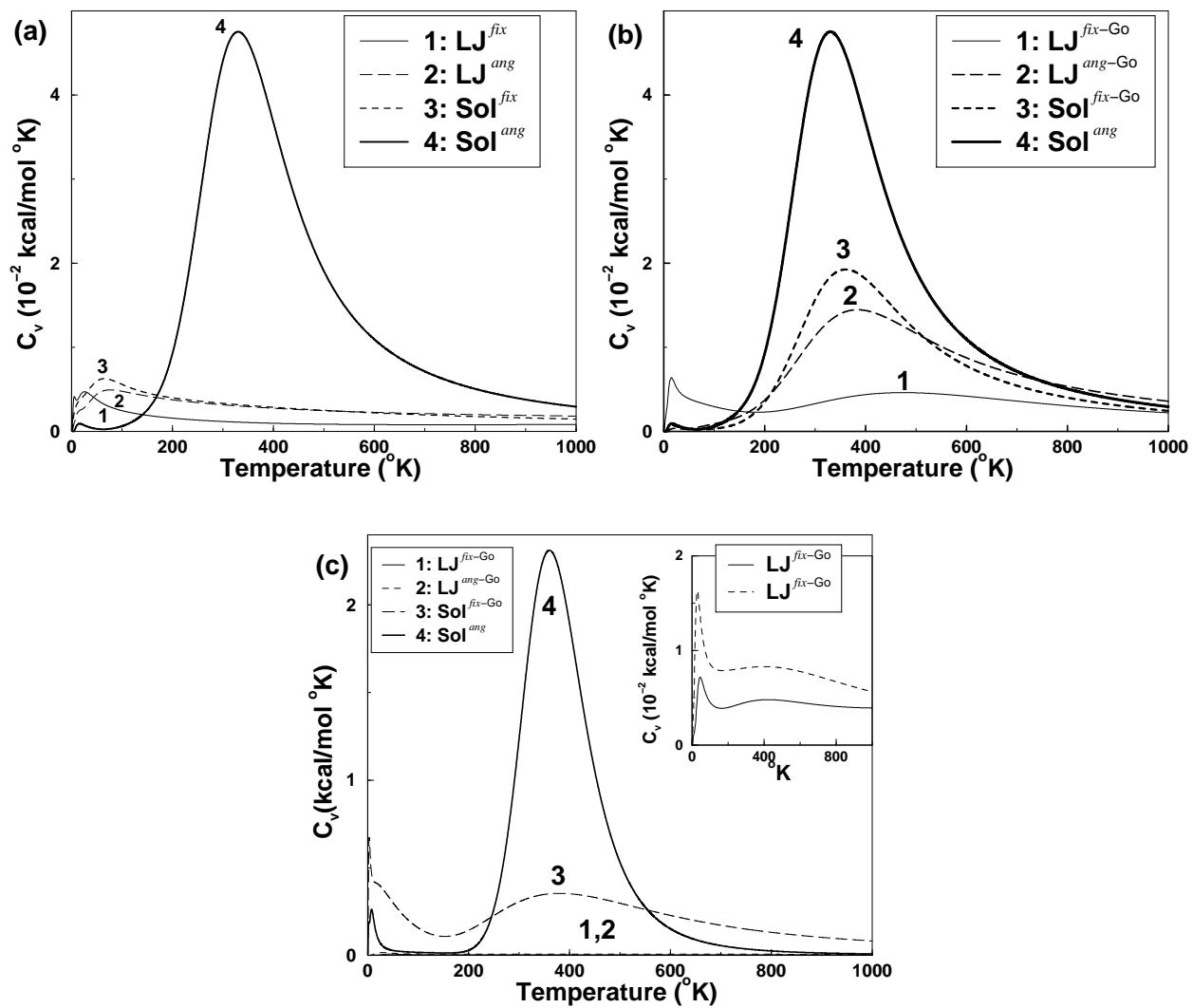


FIG. 3:

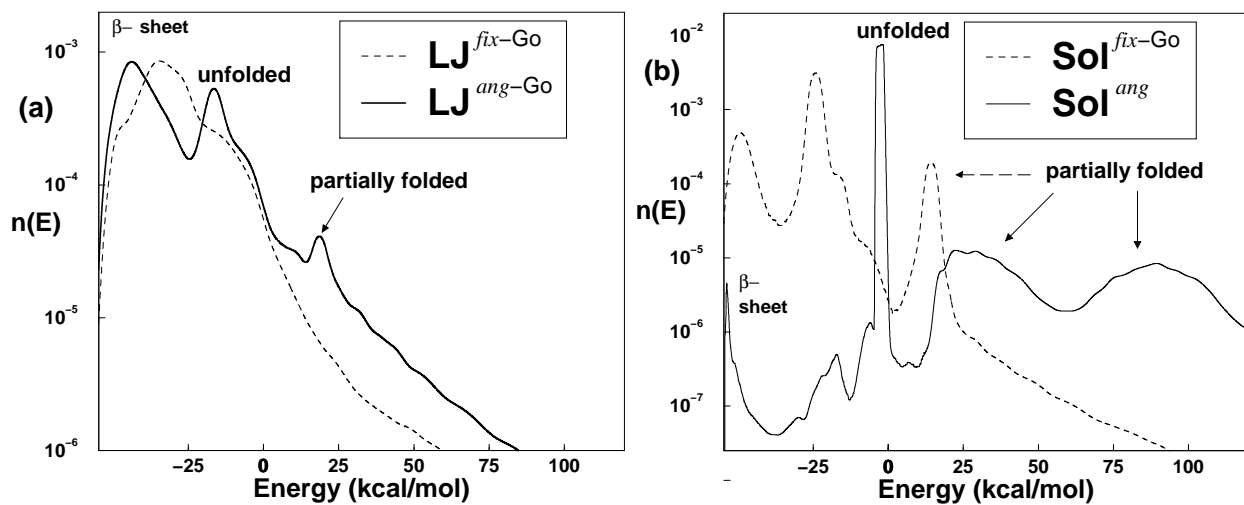


FIG. 4:

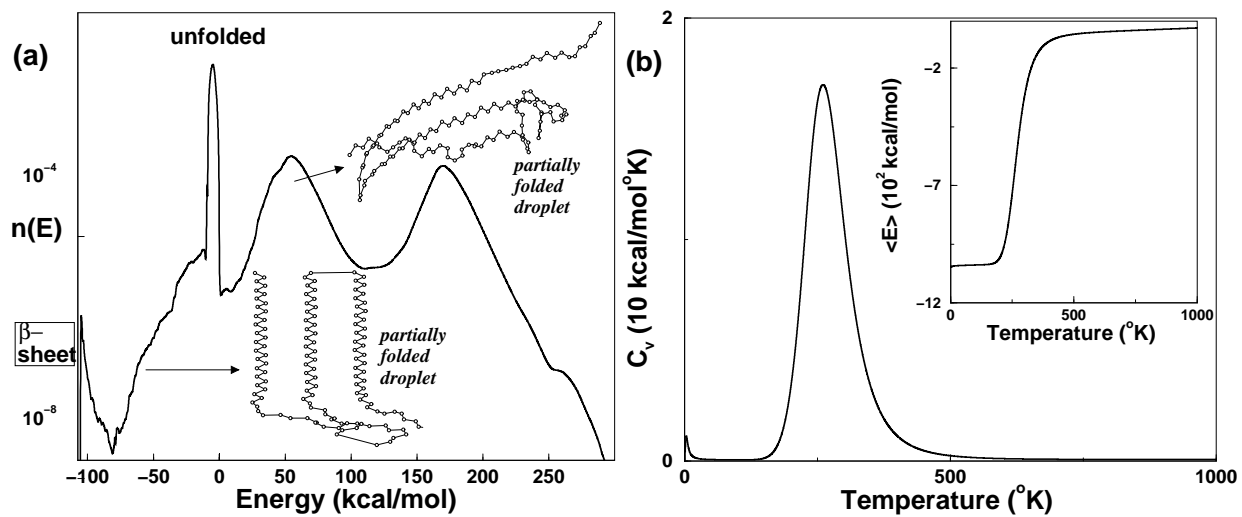


FIG. 5:

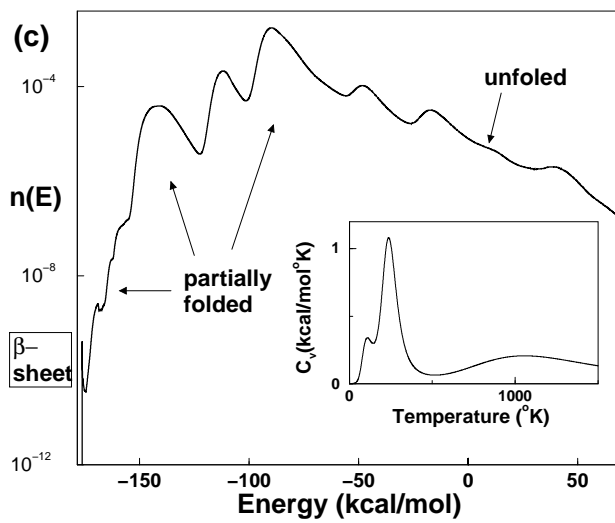
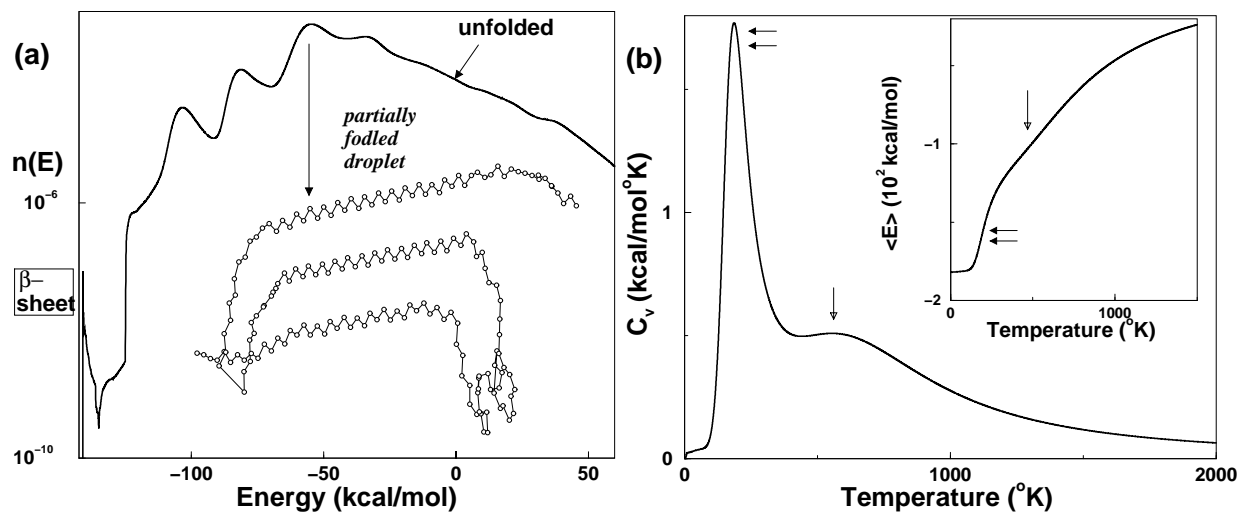


FIG. 6:

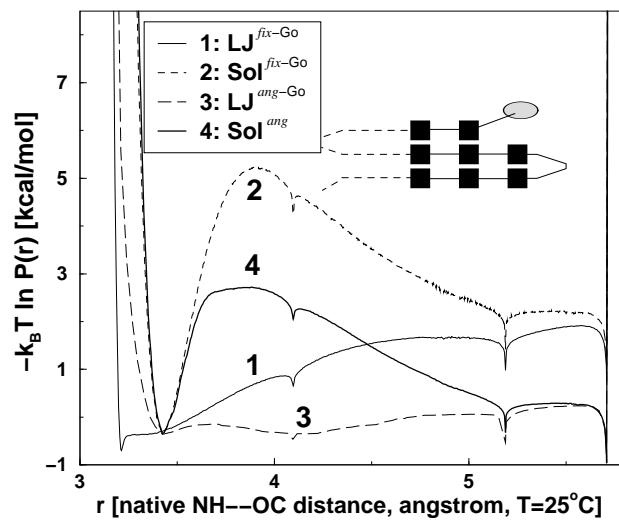


FIG. 7:

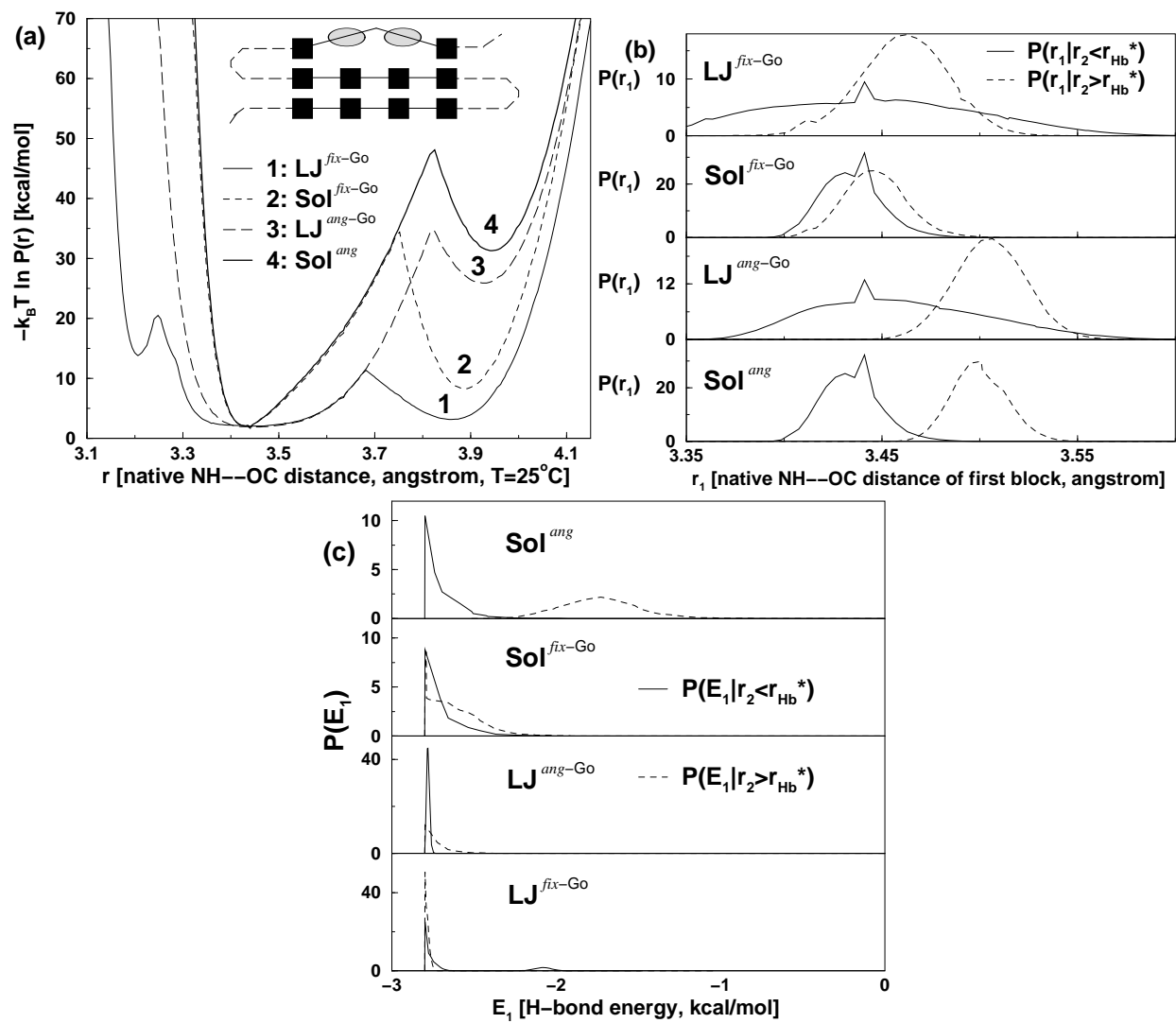


FIG. 8:

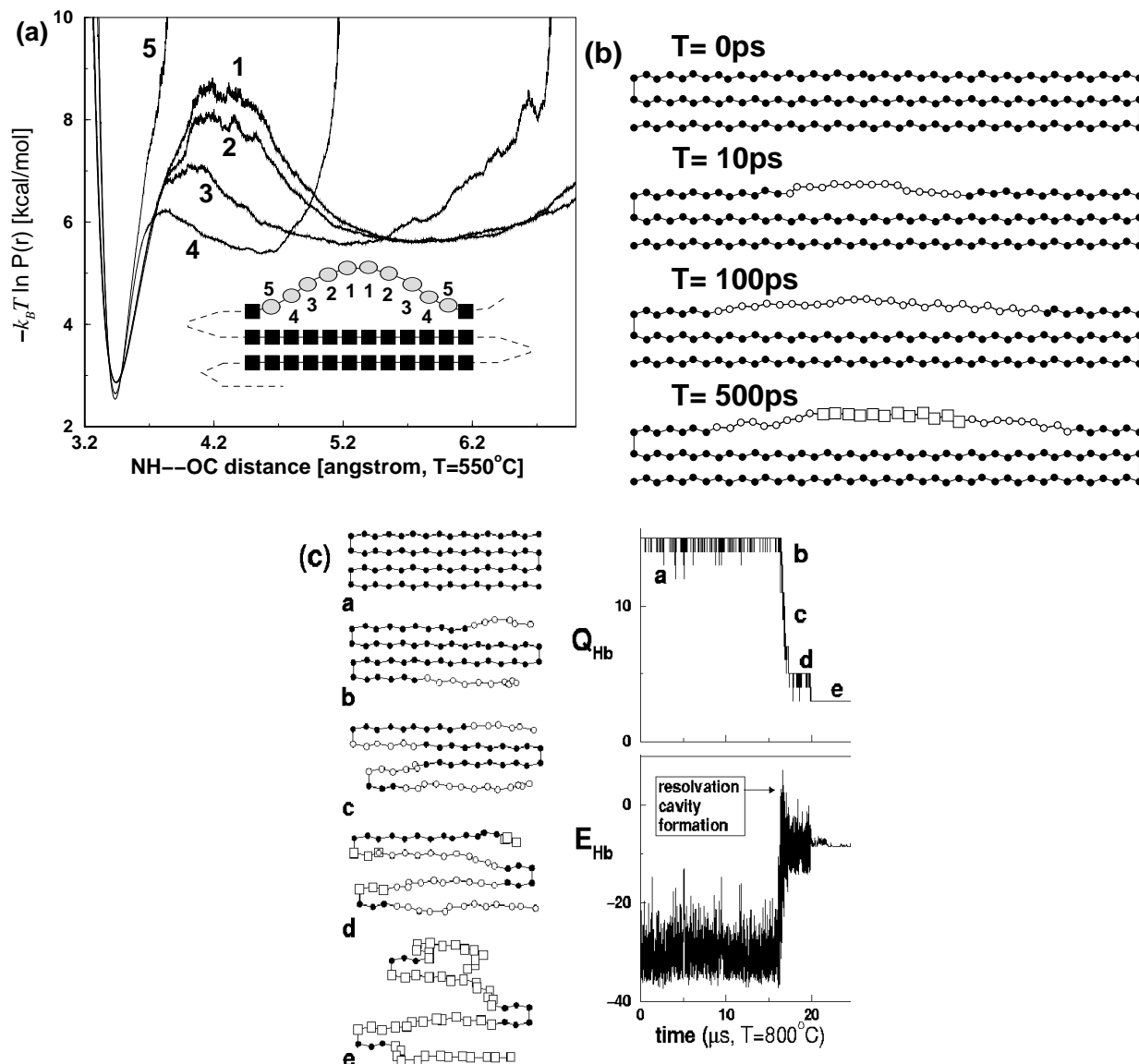


FIG. 9: